Chemical Engineering Journal 417 (2021) 127923

Contents lists available at ScienceDirect

Chemical Engineering Journal

journal homepage: www.elsevier.com/locate/cej

High-temperature pyrolysis modeling of a thermally thick biomass particle based on an MD-derived tar cracking model

Tao Chen [a,*], Xiaoke Ku [b,c], Tian Li [d,e], Bodil S.A. Karlsson [f], Jonas Sjöblom [a], Henrik Ström [a,e]

[a] Department of Mechanics and Maritime Sciences, Chalmers University of Technology, 41296 Göteborg, Sweden
[b] Department of Engineering Mechanics, Zhejiang University, 310027 Hangzhou, China
[c] State Key Laboratory of Clean Energy Utilization, Zhejiang University, 310027 Hangzhou, China
[d] RISE Fire Research, NO-7092 Tiller, Norway
[e] Department of Energy and Process Engineering, Norwegian University of Science and Technology, 7491 Trondheim, Norway
[f] RISE Research Institutes of Sweden, Division Built Environment, 41258 Göteborg, Sweden

ARTICLE INFO

Keywords:
Biomass pyrolysis
Thermally thick
Multistep kinetic scheme
MD tar cracking model
Particle-resolved simulation

ABSTRACT

Biomass pyrolysis in the thermally thick regime is an important thermochemical phenomenon encountered in many different types of reactors. In this paper, a particle-resolved algorithm for thermally thick biomass particle during high-temperature pyrolysis is established by using reactive molecular dynamics (MD) and computational fluid dynamics (CFD) methods. The temperature gradient inside the particle is computed with a heat transfer equation, and a multiphase flow algorithm is used to simulate the advection/diffusion both inside and outside the particle. Besides, to simulate the influence of intraparticle temperature gradient on the primary pyrolysis yields, a multistep kinetic scheme is used. Moreover, a new tar decomposition model is developed by reactive molecular dynamic simulations where every primary tar species in the multistep kinetic scheme cracks under high temperature. The integrated pyrolysis model is evaluated against a pyrolysis experiment of a centimeter-sized beech wood particle at 800–1050 °C. The simulation results show a remarkable improvement in both light gas and tar yields compared with a simplified tar cracking model. Meanwhile, the MD tar cracking model also gives a more reasonable prediction of the species yield history, which avoids the appearance of unrealistically high peak values at the initial stage of pyrolysis. Based on the new results, the different roles of secondary tar cracking inside and outside the particle are studied. Finally, the model is also used to assess the influence of tar residence time and several other factors impacting the pyrolysis.

1. Introduction

Biomass combustion/gasification in packed or fluidized bed reactors are important technological applications in the efforts to realize a renewable energy system [1,2]. However, due to the complicated pyrolysis behavior of biomass under high temperature conditions, efficient energy utilization is still not easy to achieve despite decades of experimental and numerical investigations. To name a few, those difficulties include tar and soot formations [3,4], which may lead to disturbances and reduced efficiency. For example, during incomplete combustion in packed-bed or fluidized-bed reactors, tar generation leads to the formation of PAHs (C_6H_6, C_7H_8, $C_{10}H_8$ etc.), which, under appropriate conditions, will further convert to soot that cause air pollution [5]. During gasification, the viscous tar species can adhere to the heat transfer surfaces of a reactor and cause fouling of the equipment that will eventually deteriorates the gasification efficiency [6]. Besides, the utilization of bio-syngas often requires a high quality of the product gas (e.g., fuel cells). Catalytic cracking of tar is a commonly-used method for the gas cleaning during gasification. The organic tar compounds, however, can also condense on the catalyst surface and form coke, which significantly reduces the catalytic activity of tar cracking in the gas cleaning process of fluidized-bed gasification [7].

Besides the traditional issues on tar generation, the large particle size used in a packed bed reactor results in a series of new problems that are mainly caused by the non-negligible temperature gradient and porous structure evolution during particle heating and devolatilization [8–10]. This issue also exposes new challenges on numerical analysis of gasification performance. The assumption that a biomass particle maintains a uniform internal temperature distribution during a thermochemical conversion process significantly simplifies the modeling procedure and is known as the thermally thin approach. However, it has long been

* Corresponding author.
E-mail address: tchen@chalmers.se (T. Chen).

https://doi.org/10.1016/j.cej.2020.127923
Received 31 July 2020; Received in revised form 30 October 2020; Accepted 26 November 2020
Available online 2 December 2020

Nomenclature

c_s	solid phase specific heat, J/(kg K)
D_{eff}	effective mass diffusion coefficient, m^2/s
e_s	emissivity, -
G	incident radiation, kg/s^3
h	solid phase heat transfer coefficient, $W/(m^2 K)$
h_s	sensible enthalpy, J/kg
m_i, m_i^s	atom mass, solid mass, kg
M_i	species molar mass, g/mol
Q	solid phase energy source term, W/m^3
$S_{p,m}$	mass source term from virtual particle, $kg/(m^3 s)$
S_h, $S_{p,h}$, S_{rad}	enthalpy source terms from gas reaction, virtual particle and radiation, W/m^3
$S_{p,mom}$	momentum source term, N/m^3
$S_{p,Yi}$, S_{Yi}	species source terms from virtual particle and gas reaction, $kg/(m^3 s)$
α_{eff}	effective thermal diffusivity, kg/(m s)
α_j	stoichiometric number, -
ε_g	gas phase volume fraction, -
κ	solid phase heat conduction coefficient, W/(m K)
σ	Stefan-Boltzmann constant, $W/(m^2 K^4)$
CELL	cellulose, $C_6H_{10}O_5$
HCE	hemicellulose, $C_5H_8O_4$
LIGC, LIGH, LIGO	lignin components, $C_{15}H_{14}O_4$, $C_{22}H_{28}O_9$, $C_{20}H_{22}O_{10}$

recognized that the thermally thin model is not suitable for large particles with Biot numbers larger than 0.1 [11], indicating that for such particles, a thermally thick approach is more appropriate [12]. Early thermally thick pyrolysis models were characterized as one-dimensional with layer evolution, where intraparticle temperature gradients result in the formation of moist, dry and char layers, respectively [13–15]. Chemical reactions and species diffusion in different layers are solved with a set of ordinary differential equations. Subsequently, traditional one-dimensional layer models were further improved by introducing meshes in each layer. These studies can be found in the works of Di Blasi et al. [16], Gómez et al. [17] and more recently Li et al. [18]. A one-dimensional model is computationally efficient. However, it is not easy to accurately account for the spatio-temporal effects of Stefan flow and gas phase tar cracking, although some works considered the intraparticle species diffusion [19]. The second type of thermally thick model is computational fluid dynamics (CFD)-based particle-resolved or pore-resolved models [20–23]. By using a CFD method, the advection and diffusion of gas species both inside and outside the particle, which plays an important role in the chemical reactions, can be captured in better detail [24]. However, such direct numerical simulations usually suffer from huge computational costs compared with the simpler one-dimensional models.

The slow temperature increase inside thermally thick particles during the initial stage of pyrolysis contributes to tar generation [25]. These tars further decompose and form light gas species under high temperature conditions [26]. The widely used one-step first-order Arrhenius pyrolysis models are not sufficient to take the influence of temperature gradients into account within the thermally thick regime, due to the prescribed stoichiometric factors for each pyrolysis product [27]. Instead, competitive pyrolysis models such as the Miller&Bellan kinetic scheme [28] and the bioCPD scheme [29] are more suitable, in which the amounts of tar and light gas are temperature-dependent variables. Moreover, in high-temperature pyrolysis, the role and fate of tar are complicated. Since the distribution of tar species in real situations depends largely on material type and heating process [30], it becomes very challenging to develop a generalized detailed tar formation model. On the other hand, however, lumped models which represent tar merely with a single species such as benzene or phenol may also loose accuracy in pyrolysis simulations where the actual natures of different tar species are important for the final product distribution. In recent years, researchers in Ranzi's group developed a multi-step kinetic scheme which achieves good balance between computational cost and accuracy [31,32]. This multi-step pyrolysis model is suitable for different types of biomasses and has been validated in a wide range of applications. In low temperature pyrolysis simulations, excellent performance has been obtained using the multi-step kinetic model [33–35].

In the study of tar generation and decomposition, despite significant experimental contributions [36], a generalized tar cracking model applicable also at high temperature is however still unavailable. Recently, some researchers have turned to microscale numerical simulations to elucidate the tar evolution mechanisms, among which reactive molecular dynamic (MD) simulation is believed to be a promising tool [37]. In a reactive MD simulation, the movement of atoms is governed by Newton's second law of motion based on a reactive force field. Molecular structure evolution is then derived straightforwardly from the chemical bond information between different atoms without any pre-assumption [38]. To name a few, Castro-Marcano et al. analyzed the structure evolution and chemical reactions of Illinois No. 6 coal by using ReaxFF MD simulation [39], and Zheng et al. carried out MD simulations in the study of cellulose pyrolysis [40]. In the latter work, the formation of active cellulose, light gas, char and tar was successfully captured. In addition, MD simulations are also reported in the study of cellulose, hemicellulose and lignin gasification [41]. However, these studies mainly focus on the explanation of the microscale pyrolysis mechanism. A global reaction model that can be easily used for macroscale simulations is still unavailable.

The purpose of this paper is to establish a high-temperature pyrolysis model for thermally thick biomass particles focusing especially on intraparticle temperature gradients and secondary tar cracking. The work is expected to be useful in the future study of biomass gasification/combustion in packed bed reactors and woodstoves. To achieve this goal, a new tar cracking model based on the multi-step kinetic scheme [31] is first developed via reactive MD simulations. The model is thereafter integrated with a previously established particle-resolved thermally thick algorithm [42]. Finally, the high temperature pyrolysis model is used to study the thermal decomposition of a centimeter-sized wood particle. Owing to their role in the particulate matter formation and fouling of equipment, the evolution of tars is a major stumbling block in the design and operation of novel thermochemical conversion concepts for biomass-based fuels. The ability to understand and control the tar evolution would significantly enhance the possibilities of large-scale adoption of such new, environmentally friendly concepts.

The structure of the paper is arranged as follows. Section 2 describes the general idea of pyrolysis modeling for a thermally thick biomass particle and the method of molecular dynamic simulation. Section 3 shows the tar thermal decomposition by using MD simulation. The integrated pyrolysis model is then validated in Section 4. After that, the influence of several parameters on the pyrolysis is discussed in Section 5. Finally, some conclusions are drawn.

2. Numerical methods

In the current work, we characterize high-temperature pyrolysis as the situation where tar cracking plays an important role, which is approximately above 500–600 °C in operating temperature [29]. During the high-temperature pyrolysis of a thermally thick biomass particle, the temperature at the particle surface increases rapidly, while the center of

the particle undergoes a slow heating process at the initial stage of pyrolysis, which results in a large amount of tar generation. As the tar species have to pass through a high-temperature region on their way out of the particle, they are further decomposed both inside and outside the particle. Therefore, in the pyrolysis of thermally thick biomass particles, light gas and tar yields are highly dependent on the intraparticle heating process. Besides, the feedback influence of the tar cracking on the pyrolysis process itself should also be considered, which includes both the Stefan flow effect and thermodynamic effects [42]. To the best of our knowledge, the derivation of computationally viable yet accurate modelling approaches to high-temperature pyrolysis of thermally thick biomass particles is still an open problem. In this section, a new modeling strategy aiming to meet the aforementioned challenges is introduced.

2.1. Primary pyrolysis of a thermally thick biomass particle

Under both low- and high-temperature conditions, the primary pyrolysis process includes moisture evaporation, devolatilization of the biomass to produce light gas and tar, as well as the formation of solid residual char. Therefore, a low temperature pyrolysis model previously developed in our group is used here as a basis for the simulation of high-temperature primary pyrolysis [42–45]. The model is established based on a particle-resolved multiphase flow algorithm, which has been systematically validated for different biomass types, particle sizes, pyrolysis temperatures and inflow velocities. The governing equations are listed in Table 1. For conciseness, only the main idea of the model is described here.

The biomass particle is modeled with two systems. To obtain the intra-particle temperature distribution, a heat transfer equation (Eq. 1) is first solved by treating the particle as a continuous system. As can be seen on the right-hand side of Eq. 1, heat conduction, heat convection, radiation and devolatilization heat are all included. For simulating the radiation, a P-1 radiation model is used [42]. With the mass loss, the biomass particle becomes a porous medium. The porosity and specific surface area of the particle evolve according to a random pore model [45]. During devolatilization, the released pyrolysis gases move through the porous structure by both diffusion and convection, forming the so-called Stefan flow. Therefore, the heat and mass transfer between the two domains both inside and outside the particle has to be considered simultaneously in the simulation. To make a uniform algorithm for the two domains, a particle-resolved multiphase flow model is used. The algorithm is realized by discretizing the porous biomass particle into a virtual particle cluster. Each virtual particle corresponds to a local heat transfer grid cell. These virtual particles together with the surrounding gas are treated as a multiphase flow system. In this way, the computation cost is reduced significantly compared with a traditional pore-resolved CFD method. The gas phase governing equations include mass, momentum and energy conservation laws (Eqs. 2–4) as well as species transport equations (Eq. 5).

In the simulation of pyrolysis, each virtual particle (representing a fraction of the solid phase) undergoes a multistep thermochemical conversion using the multistep kinetic scheme (Eq. 6). The pyrolysis starts from the thermal decomposition of the three basic components (cellulose, hemicellulose and lignin) which are pre-defined for a specific biomass type [31]. Then intermediate species are formed depending on the local temperature. Meanwhile, light gas and tar are released as primary pyrolysis products. In the gas phase, the primary tar species further crack into light gas and small molecules (Eq. 8). The primary pyrolysis gas together with the secondary tar cracking product form the source terms of the gas phase governing equations. Note that some of the previous researchers such as Blondeau et al. [46] have pointed out that the kinetic constants of the original multistep scheme should be adjusted in order to give an accurate prediction under high temperatures. In our previous work [42], we also found that the original kinetic constants result in the appearance of an unrealistic second peak in the methane production rate under high-temperature conditions. Therefore, in the current simulation, the thermal decomposition of intermediate methane into gas phase methane in the original multistep pyrolysis model is adjusted by modifying the corresponding activation energy to the same with that of intermediate CO, which alleviates the skewed production rate while imposing no influence on the amount of species yield.

Table 1
Solid phase, gas phase, primary pyrolysis and tar cracking governing equations [42].

Submodel	Governing equation	
Solid phase	$\rho_s c_s \frac{\partial T_s}{\partial t} = \nabla(\kappa \nabla T_s) + hS'(T_g - T_s) + \frac{e_s S'}{4}(G - 4\sigma T_s^4) + Q$	(1)
Gas phase	$\frac{\partial}{\partial t}(\varepsilon_g \rho_g) + \nabla\cdot(\varepsilon_g \rho_g \boldsymbol{u}_g) = S_{p,m}$	(2)
	$\frac{\partial}{\partial t}(\varepsilon_g \rho_g \boldsymbol{u}_g) + \nabla\cdot(\varepsilon_g \rho_g \boldsymbol{u}_g \boldsymbol{u}_g) = -\nabla p + \nabla\cdot(\varepsilon_g \boldsymbol{\tau}_{eff}) + \varepsilon_g \rho_g \boldsymbol{g} + S_{p,mom}$	(3)
	$\frac{\partial}{\partial t}(\varepsilon_g \rho_g E) + \nabla\cdot(\varepsilon_g \boldsymbol{u}_g(\rho_g E + p)) = \nabla\cdot(\varepsilon_g \alpha_{eff} \nabla h_s) + S_h + S_{p,h} + S_{rad}$	(4)
	$\frac{\partial}{\partial t}(\varepsilon_g \rho_g Y_i) + \nabla\cdot(\varepsilon_g \rho_g \boldsymbol{u}_g Y_i) = \nabla\cdot(\varepsilon_g \rho_g D_{eff} \nabla Y_i) + S_{p,Y_i} + S_{Y_i}$	(5)
Primary pyrolysis	$\frac{dm_i^s}{dt} = A_i exp\left(-\frac{E_i}{RT}\right) m_i^s \quad i = CELL, HCE, LIGC, LIGH, LIGO$	(6)
	$M_i^s \rightarrow \sum \alpha_j M_j^p, \quad j = light\ gas, tar, intermediate\ species, char$	(7)
Tar cracking	$M_i^{tar} \rightarrow \sum \alpha_j M_j^g,\ j = H_2, CH_4, CO, CO_2 \ldots$	(8)

2.2. Secondary tar decomposition

The multistep kinetic scheme developed by Debiagi et al. [31] has shown good performance in low-temperature pyrolysis simulations for thermally thick biomass particles [33,42]. However, an efficient tar cracking model that extends the application of the multistep kinetic scheme to high-temperature pyrolysis is still missing. Although a simplified model was developed by Blondeau et al. (Table 2) and used by many other researchers [46], a great discrepancy with experimental measurements was found in the application of thermally thick biomass particle pyrolysis, where the decomposition rate and CO_2 generation were significantly overpredicted [42].

As can be seen in the simplified tar cracking model, the decomposition of each tar species generates no more than three light gas species, and the kinetic constants are the same for all the reactions. These assumptions are sufficient to accomplish a decomposition into the dominating permanent light gas components, but too rough to capture the real kinetic process of tar cracking. Therefore, it is necessary to develop a more advanced tar cracking model. In this paper, a ReaxFF molecular dynamics (MD) method, which was originally developed by van Duin et al. based on an atomic-scale bond-order theory [38], is utilized. Generally, the ReaxFF force field provides a continuous description of interatomic potential (Eqs. 9–10) and is capable of describing chemical bond formation and dissociation. In our simulation, the same ReaxFF force field as that of Castro-Marcano et al. [39] is used to develop the secondary tar cracking model.

Table 2
Simplified kinetic scheme of tar decomposition [46].

Reactions	A (1/s, $\times 10^6$)	E (kJ/mol)
HMFU → $3CO + 1.5C_2H_4$	4.28	108
$C_3H_6O \rightarrow 0.5CO_2 + 0.5H_2 + 1.25C_2H_4$	4.28	108
pCoumaryl → $CO_2 + 2.5C_2H_4 + 3Char$	4.28	108
Phenol → $0.5CO_2 + 1.5C_2H_4 + 2.5Char$	4.28	108
XYLOSE → $2CO_2 + H_2 + 1.5C_2H_4$	4.28	108
LVG → $2.5CO_2 + 1.5H_2 + 1.75C_2H_4$	4.28	108
HAA → $2CO + 2H_2$	4.28	108
Glyoxal → $2CO + H_2$	4.28	108
Lumped Phenol → $2CO_2 + 3C_2H_4 + 3Char$	4.28	108

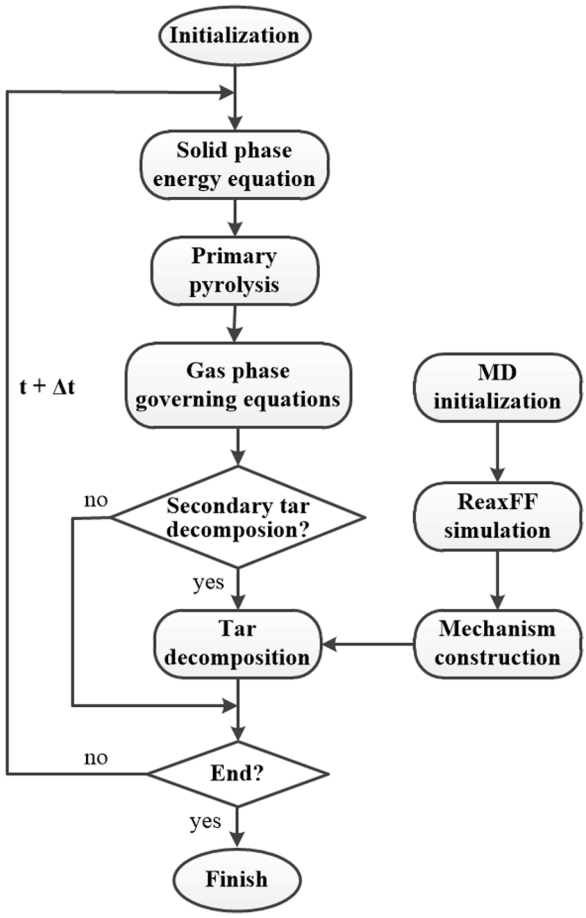

Fig. 1. High-temperature pyrolysis algorithm for thermally thick biomass particles.

$$m_i \frac{d^2 \boldsymbol{x}_i}{dt^2} = -\frac{dE_{system}(\boldsymbol{x})}{d\boldsymbol{x}} \tag{9}$$

$$E_{system} = E_{bond} + E_{over} + E_{under} + E_{val} + E_{pen} + E_{tors} + E_{conj} + E_{vdWaals} + E_{Coulomb} \tag{10}$$

E_{bond} on the right-hand-side of Eq. (10) is the bond energy, E_{over} and E_{under} are coordination correction terms, E_{val}, E_{pen}, E_{tors} and E_{conj} represent the valence angle energy, penalty energy, torsional energy and conjugation energy, respectively. The last two terms are non-bonded Van der Waals and Coulomb interactions. The details of the new tar cracking model derived from the MD simulations are provided in Section 3.

2.3. Integrated algorithm of the pyrolysis model

Fig. 1 shows the integrated high-temperature pyrolysis algorithm for thermally thick biomass particles. The model is established as follows. Firstly, a new tar cracking model is developed through MD simulation. A molecular pyrolysis system for each of the representative tar species (Table 3) in the multistep kinetic scheme [31] is constructed. Then, the thermal decomposition products and the corresponding kinetic rate of the new tar cracking model are derived from the instantaneous information of the pyrolysis system. The integrated pyrolysis model is implemented in the OpenFOAM software [47], and constitutes an extended version of the low-temperature pyrolysis algorithm of our previous work [42]. During each time step, the solid phase energy equation is solved first. The intraparticle temperature distribution is then transferred to the virtual particle system based on which primary pyrolysis occurs. The released products from primary pyrolysis are used to update the source terms of gas phase governing equations. After the new information is updated in the flow field, secondary tar decomposition is computed according to the MD tar cracking model. Note that in Fig. 1, the tar cracking module can be switched off based on a user-defined temperature threshold (e.g. 500 °C), which could save computational costs in low-temperature simulations. The implementation of the whole algorithm is based on the standard second-order spatial and temporal discretization algorithms in OpenFOAM. Besides, an MPI strategy is used for parallelization of the simulation.

3. Tar decomposition model

In this section, MD simulations are carried out to construct a tar decomposition model. Before the MD simulation, a periodic computational cell with the density of 0.1 g/cm^3 containing 1000 molecules are created for each tar species by a procedure similar to that in Zheng et al. [40], where the following three major steps are implemented. First, the molecular geometry is optimized by using a conjugate gradient algorithm in the Materials Studio software [48], based on which the cell system is constructed. Then, an annealing procedure with a temperature variation from 300 to 500 K is carried out for the periodic system. Finally, the system is equilibrated at 500 K in the LAMMPS software [49]. The ReaxFF MD simulation is also implemented in LAMMPS by using NVT ensemble (particle number (N), system volume (V) and temperature (T) are conserved), and Berendsen thermostat is used to control system temperature. To derive the pre-exponential factor and

Table 3
Tar species from the multistep kinetic scheme [31].

CH_2O	HCOOH	CH_3OH	$C_2H_2O_2$	C_2H_5OH	CH_3CHO	$C_2H_4O_2$	C_3H_6O
	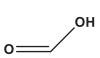		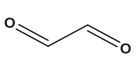	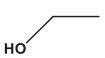		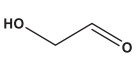	

$C_5H_8O_4$	C_6H_6O	$C_6H_6O_3$	$C_6H_{10}O_5$	C_7H_8O	$C_9H_{10}O_2$	$C_{11}H_{12}O_4$
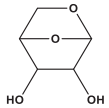	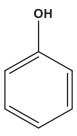	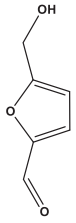	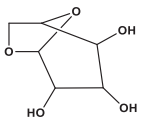	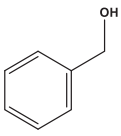	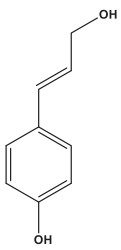	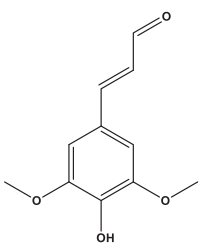

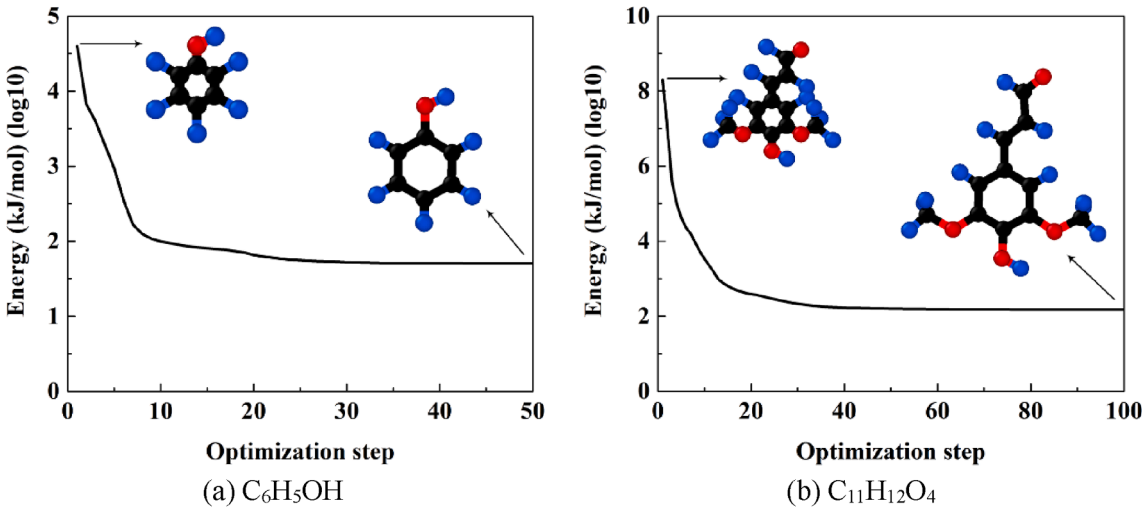

Fig. 2. Energy change during the geometry optimization (particle type: blue - H, red - O, black - C). (For interpretation of the references to colour in this figure legend, the reader is referred to the web version of this article.)

activation energy of the thermal decomposition rate, MD simulations are run under six temperature conditions ranging from 2000 to 3000 K with an interval of 200 K. For the reaction rate, a first-order Arrhenius type equation is assumed. The derivation of the kinetic constants is shown in Eq. (11), where N_0 and N_t are the initial tar molecule number and the equivalent left molecules at time instant t, respectively. A and E are pre-exponential factor and activation energy.

$$k = \frac{lnN_0 - lnN_t}{\Delta t} = Aexp(-\frac{E}{RT}) \tag{11}$$

As shown in Table 3, the primary tar species from the multistep kinetic scheme include phenol, xylose monomer and so on. Here, all of the pyrolysis products except for H_2, CH_4, CO, CO_2 and C_2H_4 are considered as candidates to experience secondary decomposition under high temperature condition. Considering the computational efficiency in the subsequent CFD simulation and the uncertainty about possible influences of the elevated temperature on the reaction dynamics, the current work is not primarily aimed at a detailed (intrinsic) tar cracking model. Instead, a lumped global cracking mechanism is established. In the new model, tar species decompose partly into steam, light gases including H_2, CH_4, CO, CO_2, C_2H_4 and the smaller hydrocarbon molecule CH_2O. The remaining decomposition products from the MD simulations are lumped as C_2H_2. The stoichiometric factors of light gases and CH_2O are determined by averaging the MD simulation results under different pyrolysis temperatures, while the values for steam and C_2H_2 are obtained by ensuring mass conservation between product and reactant.

Note that the methodology of performing the MD simulations at elevated temperatures (in comparison to the typical process temperatures) is a commonly used strategy to accelerate reactive dynamics to avoid unacceptably long simulation times [50–53]. For example, Chenoweth et al. [53] raised the simulation temperature to above 2000 K in the pyrolysis simulation of JP-10 fuel. They found that the derived activation energy from MD simulation is very close to the experimental measurement (58.4 kcal/mol predicted vs. 62.4 kcal/mol in experiment). However, the derived pre-exponential factor is much larger than the experimental data. Strictly speaking, the kinetics may indeed be different at different operating temperatures [54], which may affect the product distributions [50]. Nevertheless, temperature acceleration has been shown to produce good qualitative results for the initial decomposition process and reaction products in previous studies [40,52], attesting to the feasibility of this strategy. In the current work, we choose to remain agnostic about whether the high-temperature kinetics directly correspond to the actual kinetics, and by varying the temperature

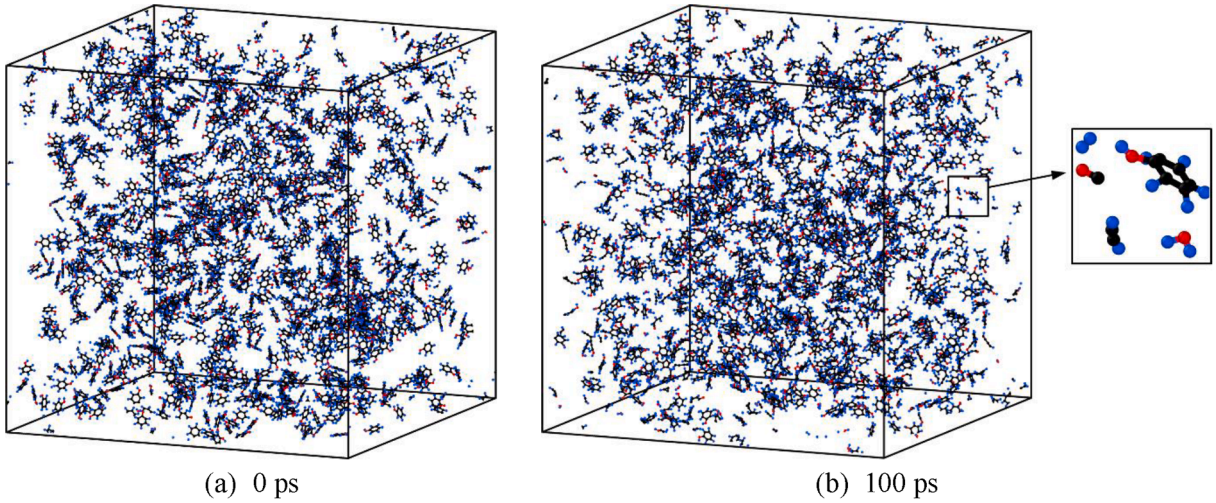

Fig. 3. Snapshots of phenol thermal decomposition at 2600 K (particle type: blue - H, red - O, black - C). (For interpretation of the references to colour in this figure legend, the reader is referred to the web version of this article.)

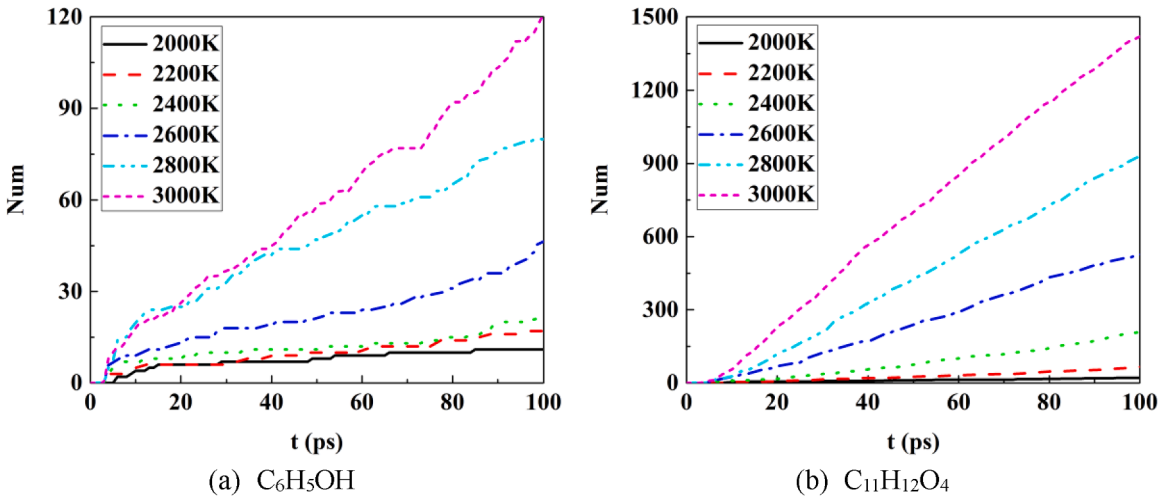

Fig. 4. Number of CO molecules generated at the initial stage of pyrolysis.

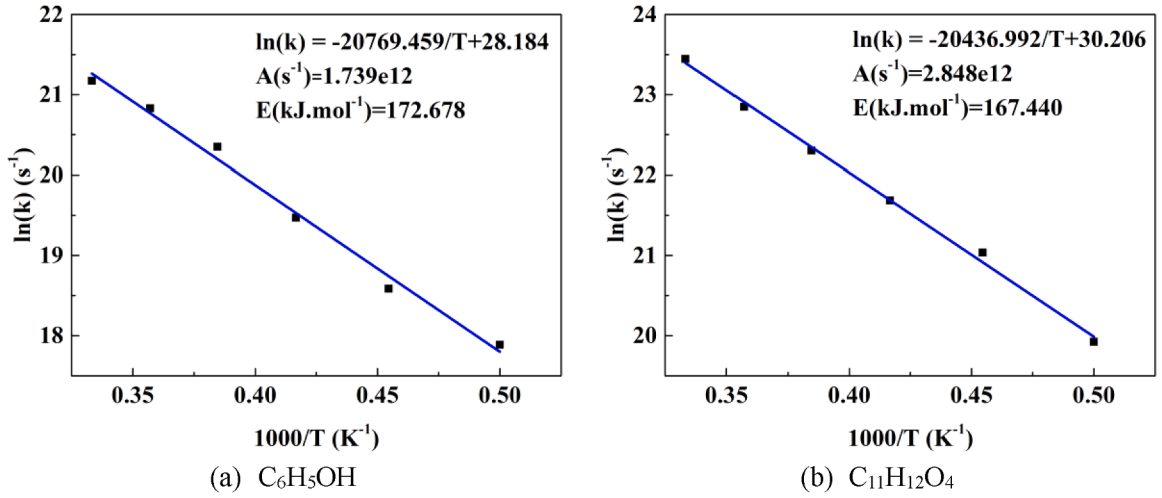

Fig. 5. Fitted thermal decomposition rate from MD simulations.

elevation we extract the initial decomposition behavior in the high-temperature limit. The method as such contains no fitting to experimental data and we thus propose that its success or failure should be evaluated on the basis of the predictions it produces in the integrated algorithm.

Fig. 2 presents the energy change during the geometry optimization of C_6H_5OH and $C_{11}H_{12}O_4$ molecules. It is seen that the molecular energy converges very quickly within 100 optimization steps, and the corresponding molecular structure also reaches an optimized conformation. The configurations of the phenol system at $t = 0$ and 100 ps at the temperature of 2600 K are shown in Fig. 3. In Fig. 3a, phenol is the only species present, whereas in Fig. 3b, small molecules such as CO and C_2H_2 can be identified. Furthermore, some large molecules like C_7H_8O are also formed, which will likely contribute to the formation of soot precursors. However, soot formation is a challenging issue which lies beyond the scope of the present research. All such polycyclic aromatic hydrocarbons are therefore lumped into C_2H_2 and steam. Fig. 4 shows the evolution of CO molecules for C_6H_5OH and $C_{11}H_{12}O_4$ under different temperatures. Fig. 5 gives the kinetic constants of C_6H_5OH and $C_{11}H_{12}O_4$ decompositions derived from the linear curve fitting of the MD simulation results. It is seen that a good linear correlation is obtained

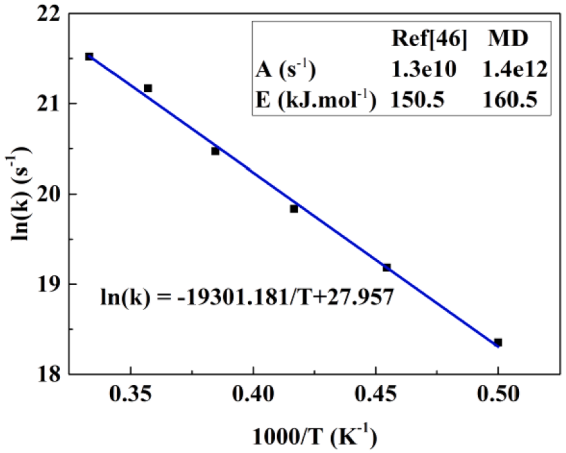

Fig. 6. Fitted cellobiose pyrolysis rate from MD simulation and comparison with that of active cellulose [46].

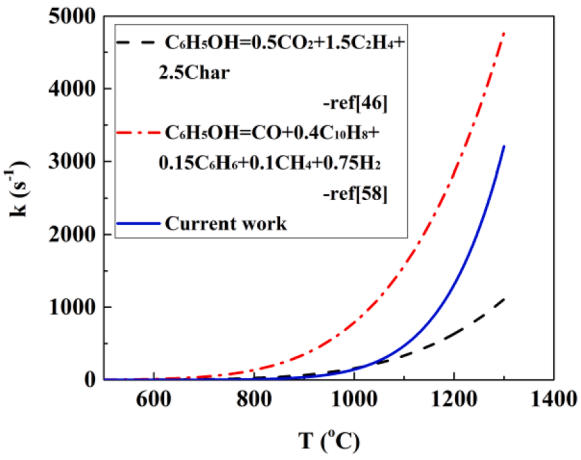

Fig. 7. Thermal decomposition rates of phenol [46,58].

between the logarithm of reaction rate and temperature reciprocal.

To demonstrate the influence of the temperature elevation strategy on the derived pyrolysis kinetics, an additional MD simulation of cellobiose ($C_{12}H_{22}O_{11}$) pyrolysis is carried out, which is studied as a model compound of active cellulose [55]. The simulation system is constructed by using the same procedure as that described previously. Fig. 6 presents the fitted cellobiose pyrolysis kinetics and the comparison with that of active cellulose. It is shown that the derived activation energy is 160.5 kJ/mol which is very close to the value 150.5 kJ/mol of active cellulose. However, the pre-exponential factor is about two orders of magnitude larger than the literature data [46]. We note here that the pre-exponential factor, although constant over limited temperature intervals, typically has a temperature dependence and increases with temperature. It is also known to vary several orders of magnitude with conversion in e.g. pyrolysis of various biomasses [56] or thermal decomposition of biodiesel constituents [57]. We therefore attribute the discrepancy in the rate mainly to the uncertainty in the determination of the pre-exponential factor caused by the temperature elevation strategy and the focus on the initial decomposition behavior. It is also not impossible that the accuracy of the reactive force field used in the MD simulation plays a minor role, but this represents an intrinsic problem of reactive MD methods and is beyond the scope of the present study.

From the above comparison and the work of Chenoweth et al. [53], one can see that, at an elevated temperature, the MD-derived activation energy is trustworthy, while the pre-exponential factor needs to be adjusted. Actually, we also found that the derived tar cracking rate from the MD simulations is much higher than the available literature values in high-temperature situations. Therefore, we modified the kinetic rates of tar decomposition by scaling the pre-exponential factors with a constant coefficient in the subsequent CFD simulations. Fig. 7 compares the modified phenol decomposition rate with that of simplified mechanism [46] and Su et al. [58] when the scaling factor is set to 1.0e-3. It is shown that, after the scaling, the MD tar cracking rate lies between the literature values. The new tar cracking model together with the modified reaction rates for all of the tar species are summarized in Table 4. The influence of the pre-exponential scaling factor on the pyrolysis yield will be further discussed in Section 5. Note that the new tar cracking

Table 4
Lumped tar cracking mechanism from MD simulations: Tar → $a_1H_2O + a_2H_2 + a_3CH_4 + a_4CO + a_5CO_2 + a_6C_2H_2 + a_7C_2H_4 + a_8CH_2O$.

Species	H_2O	H_2	CH_4	CO	CO_2	C_2H_2	C_2H_4	CH_2O	A (1/s, $\times 10^9$)	E(kJ/mol)
CH_2O	0	1	0	1	0	0	0	0	9.58	248.12
HCOOH	0.6	0.2	0	0.4	0.4	0	0	0.2	12.11	192.40
CH_3OH	0.5	0.3	0.35	0.15	0	0	0.075	0.35	79.44	244.76
$C_2H_2O_2$	0.4	0.15	0	1.2	0.1	0.25	0	0.2	15.58	211.99
C_2H_5OH	0.5	0.7	0.2	0.2	0	0.2	0.45	0.3	5.57	196.27
CH_3CHO	0.3	0.45	0.2	0.55	0	0.4	0.15	0.15	18.85	226.64
$C_2H_4O_2$	0.7	0.25	0.1	0.7	0.1	0.25	0.1	0.4	3.68	166.73
C_3H_6O	0.2	0.55	0.5	0.7	0	0.55	0.3	0.1	15.10	202.59
$C_5H_8O_4$	1.2	0.75	0.2	1.9	0.3	0.95	0.2	0.3	33.11	234.95
C_6H_6O	0	0.35	0.1	1	0	2.45	0	0	1.74	172.68
$C_6H_6O_3$	0.3	0.7	0.2	2.5	0.1	1.6	0	0	2.40	165.05
$C_6H_{10}O_5$	1.6	0.85	0.4	2	0.5	1.35	0	0.4	6.89	169.96
C_7H_8O	0	0.85	0.1	1	0	2.95	0	0	14.18	229.68
$C_9H_{10}O_2$	0	1.35	0.1	2	0	3.45	0	0	47.16	252.39
$C_{11}H_{12}O_4$	0	2.2	0.2	4	0	3.4	0	0	2.85	167.44

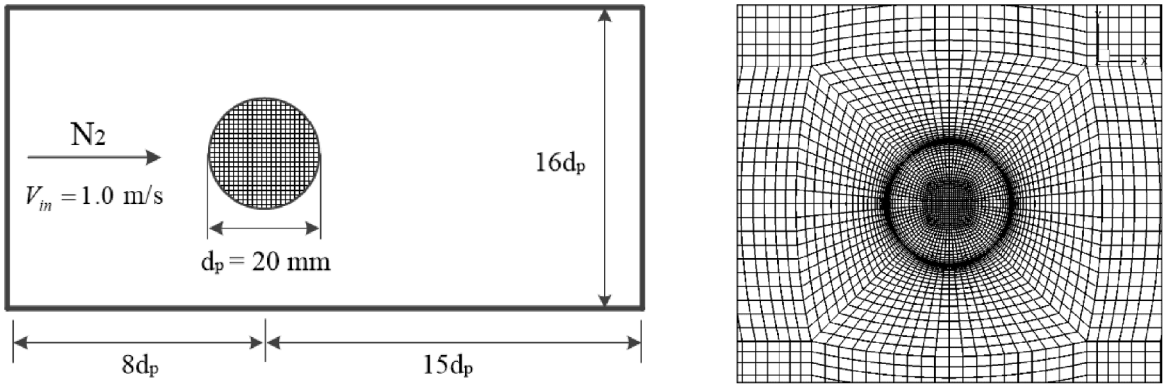

Fig. 8. Computational setup for the pyrolysis simulation of the beech wood particle [42].

Table 5
Component mass fraction of the beech wood particle (%) [31].

Biomass		Lignocellulose	
moisture	0.0	cellulose	48.85
ash	1.01	hemicellulose	21.01
lignocellulose	98.99	LIG-H	5.51
		LIG-O	18.65
		LIG-C	4.97

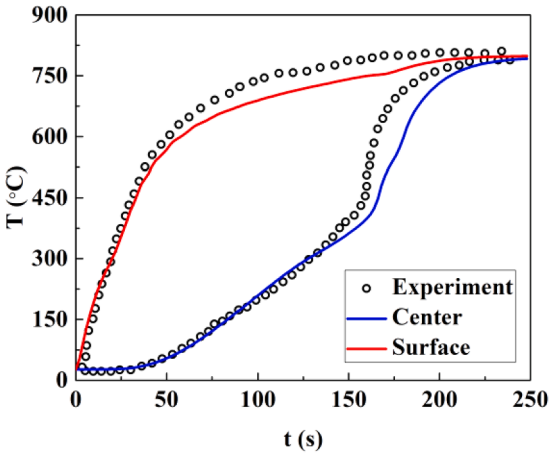

Fig. 9. Particle temperature evolution history.

mechanism does not include PAHs and char species as shown in the simplified model (Table 2), since in the MD simulation, we are only focused on the initial stage results, where soot and char have not formed yet. The formation of soot or char species (which usually happens in the final stage of soot formation) from tar cracking can be realized by either simply considering the thermal decomposition of C_2H_2 into carbon and hydrogen or using a more complex mechanism [59,60]. These works will be carried out in our future research.

4. Pyrolysis of a beech wood particle

In this section, the integrated high-temperature pyrolysis model based on the MD tar cracking mechanism is used to study the pyrolysis of a centimeter-sized beech wood particle in a nitrogen atmosphere [61]. We stress that the current work mainly focuses on the influence of tar cracking, and thus other phenomena such as catalytic effects from inorganic ash constituents and soot formation are ignored. Our main ambition is to test the hypothesis that the herein outlined MD approach can be used to derive a useful kinetic scheme for the secondary tar cracking during biomass pyrolysis. Moreover, due to that the enthalpy changes of pyrolysis reactions measured in experiment vary a lot depending on different experimental conditions [62], devolatilization heat is usually determined empirically in numerical simulations [33,46], which is rather arbitrary when it comes to the multistep pyrolysis model with many reactions. Therefore, the devolatilization heat is not considered in the current simulations. Besides, the reaction heat due to secondary tar cracking is automatically calculated by the standard OpenFOAM chemical reaction solver based on the thermophysical property of each gas species.

Fig. 8 shows the simulation setup and grid system. The computational grid inside the particle is used for the computation of both solid phase heat transfer equation and gas phase governing equations. Besides, to save computational cost, a two-dimensional simplification which has been systematically validated is used [42–45]. Grid independence studies can also be found in these works. The component analysis of the biomass material is listed in Table 5. In the simulation, the initial porosity of the particle is set to a uniform value of 0.2 [33,42]. The corresponding parameter uncertainty study, which is not replicated here for conciseness, can be found in our previous work [45]. Besides, in order to fit the heating process with the experimental measurement, the initial specific surface area is assumed to be 6000 m^2/m^3, which is equivalent to the value obtained by scaling up of a micron-sized porous biomass particle [63] (a commonly used strategy in pore-resolved direct numerical simulations [64]). Moreover, instead of introducing a secondary cooling flow in the downstream region of the furnace, as used for tar collection in the experiment, an inflow velocity of 1.0 m/s is assumed in the simulation to realize a short residence time of tar in the high-temperature domain. The influence of inflow velocity, and thus tar residence time, as well as the initial specific surface area on the pyrolysis product distribution will be further discussed in the following section.

The pyrolysis simulation is first carried out at 800 °C, which is set as a base case in this study. Fig. 9 shows the comparison of the particle heating process with the experimental measurement, in which the surface temperature is accounted by averaging the circumferential values at 2 mm from the particle surface [61]. Initially, a fast temperature rise is observed near the particle surface, while the particle center temperature remains around 27 °C for nearly 50 s. After that, the center region heating process is accelerated and the surface temperature increase is slowed down due to the Stefan flow effect caused by both primary

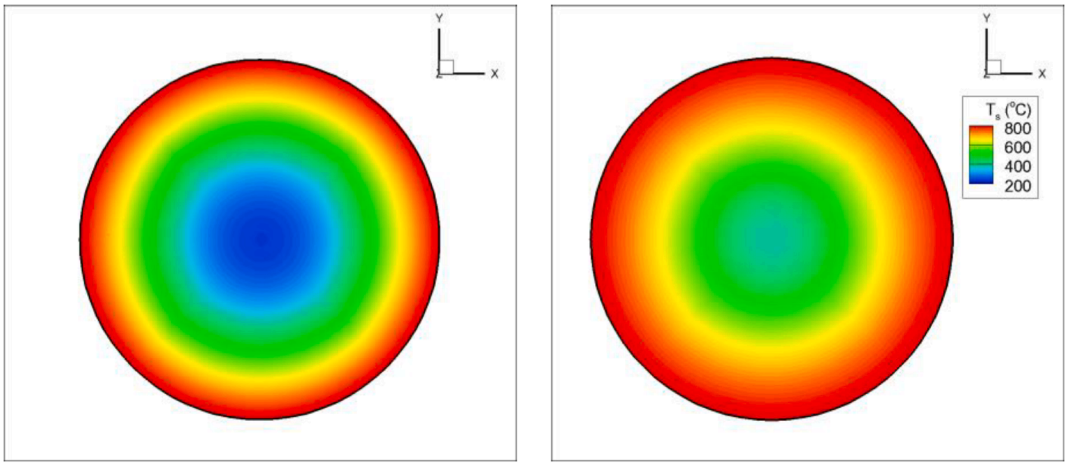

(a) t = 100 s (b) t = 150 s

Fig. 10. Particle temperature distribution.

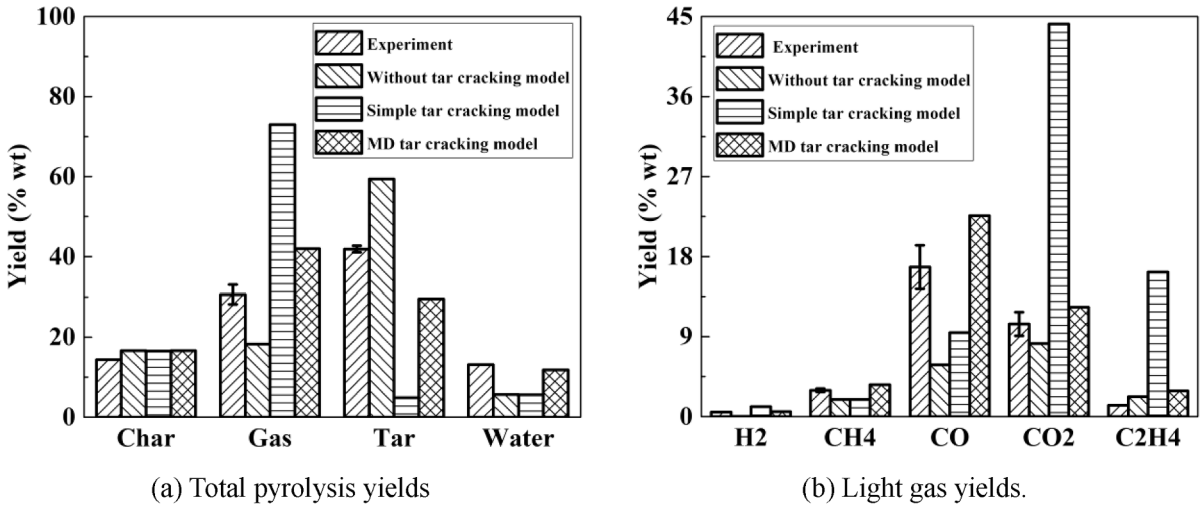

Fig. 11. Pyrolysis yields at 800 °C.

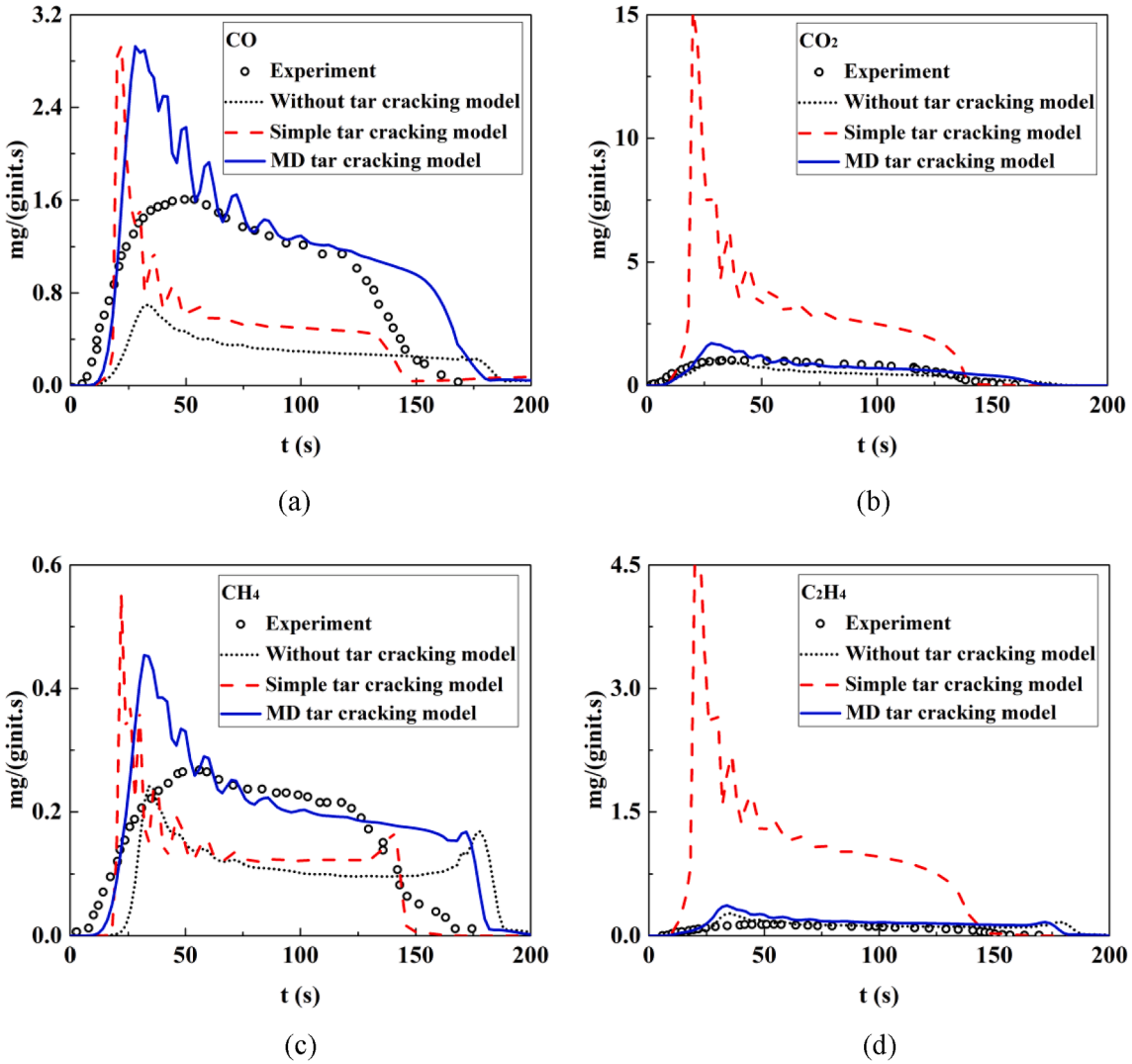

Fig. 12. Light gas production history (ginit: initial particle mass with the unit of gram).

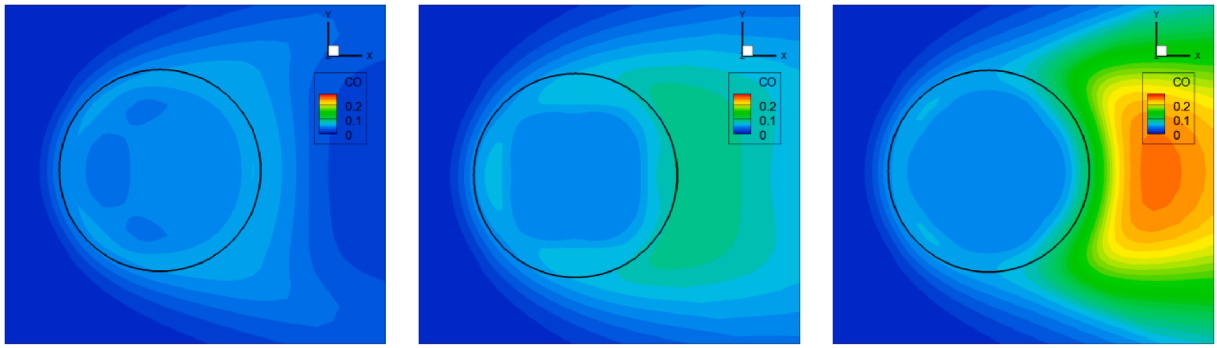

Fig. 13. CO mass fraction distribution at $t = 50$ s.

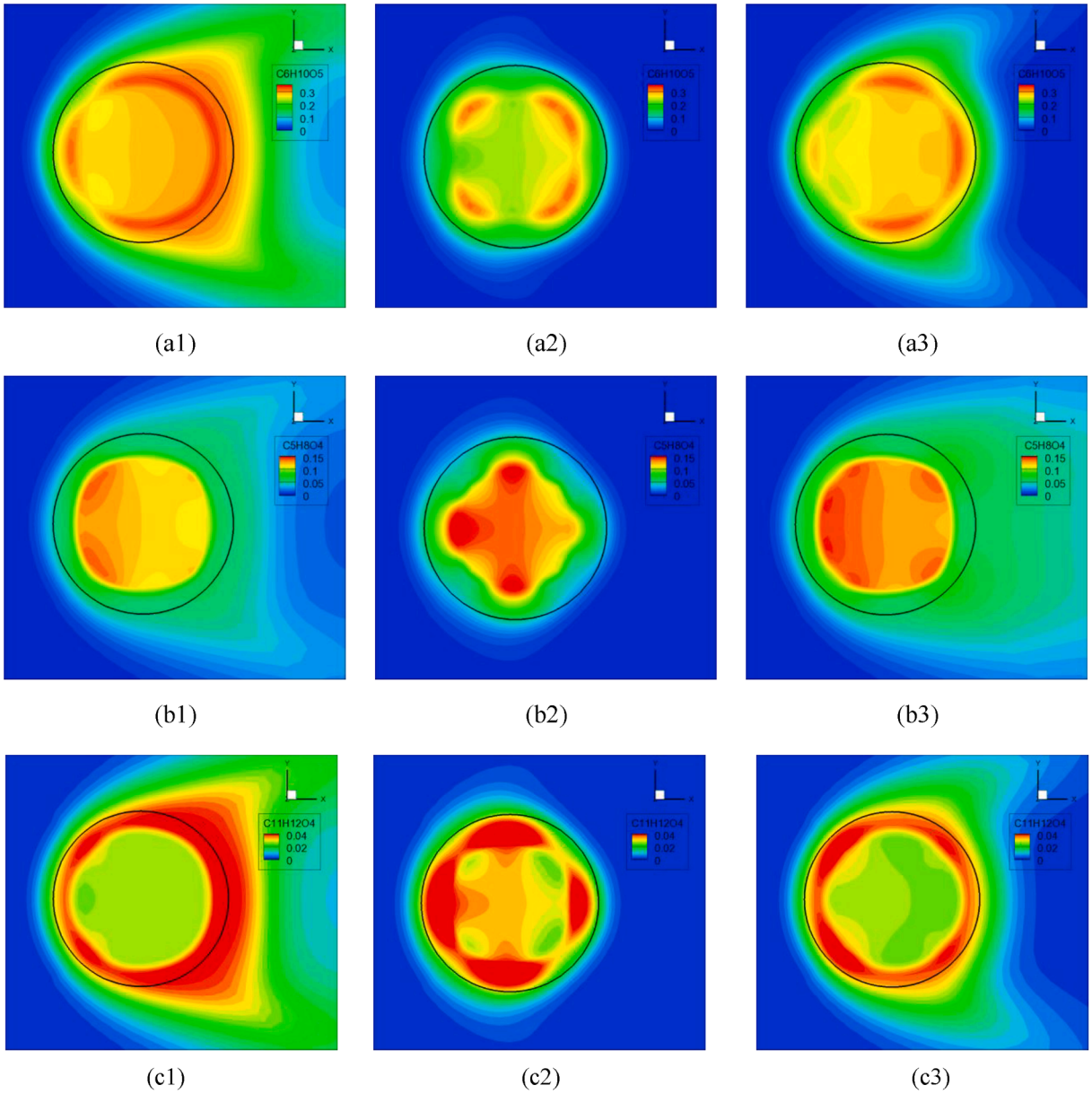

Fig. 14. Mass fraction distributions of (a) $C_6H_{10}O_5$, (b) $C_5H_8O_4$ and (c) $C_{11}H_{12}O_4$ at $t = 50$ s (x1: without tar cracking model; x2: simple tar cracking model; x3: MD tar cracking model).

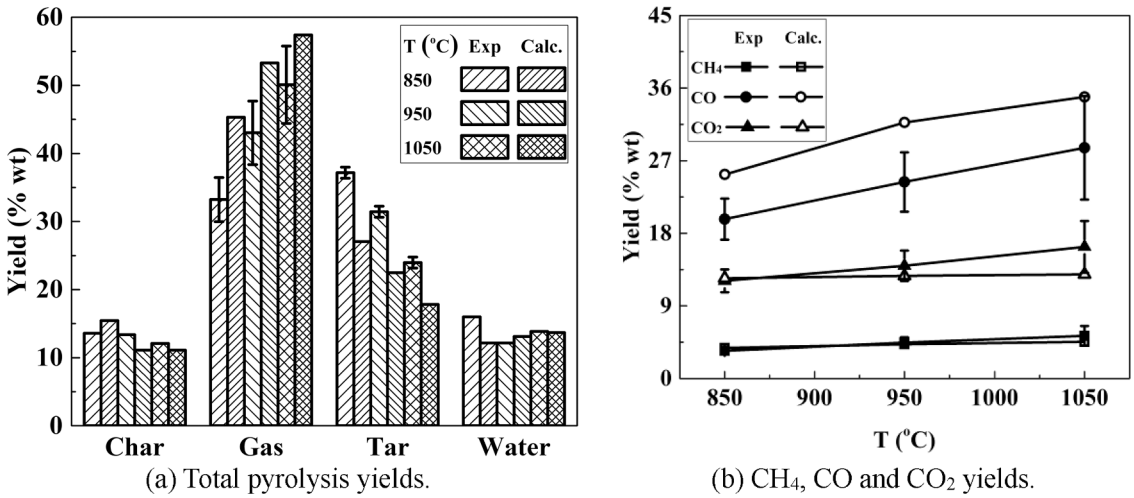

Fig. 15. Product yields at different pyrolysis temperatures.

pyrolysis and secondary tar cracking. At the end of pyrolysis, a rapid temperature increase in the particle center is also captured by the simulation. In general, the predicted particle center and surface temperatures correspond well with the experimental data. To get a further insight on the heating up process, Fig. 10 presents the temperature contours inside the biomass particle at $t = 100$ and 150 s. It is seen that the temperature distribution is almost symmetric in the circumferential direction during the heating process.

To assess the results of the MD tar cracking model, Fig. 11 compares the predicted pyrolysis yields and light gas generation with those of the original, simple tar cracking model. The char yield is computed by accounting for the complete solid content left after pyrolysis, which includes both carbon and ash. Gas species contain H_2, CH_4, CO, CO_2 and C_2H_4, while the tar yield is obtained by a differencing method. From Fig. 11a, both the simple and MD tar cracking models predict the same char yield of 17%, which is a little bit higher than the experimental result. For the light gas yield, the prediction of the simple tar cracking model increases from 18% to 73% due to secondary tar decomposition, which is more than double that of the experimental measurement (31%). The predicted value with the MD model is 42%, thus showing a significant improvement compared with the simpler model. Besides, it is also seen that the MD model produces a much better prediction of the steam yield. These improvements also result in a more reasonable prediction of the overall tar yield. In Fig. 11b, it is clearly observed that the MD model greatly improves the prediction of light gas composition. Specifically, the CO yield increases from 6% (without considering tar cracking) to 23%, which is close to the measured value of 17%. For CO_2, the MD tar cracking model also predicts a similar yield compared with the experimental data. However, the simple tar cracking model overestimates the CO_2 yield by nearly a factor of three. Besides the main gas contents, the MD model also shows an improved yield prediction of H_2, CH_4 and especially C_2H_4.

Fig. 12 presents a further comparison of the time-resolved species yield history, as observed at the outlet boundary. From Fig. 12a, a high peak value which is nearly double the experimental measurement in CO production rate is observed for the simple tar cracking model. After about 25 s, the curve drops sharply below 0.8 mg/ginit.s which is much lower than the experimental data. At the same time, the MD tar cracking model gives almost the same CO generation rate as that in the experiments after 50 s. In general, although the MD model also overpredicts the CO production rate, its result is much better than that of the simple model. In Fig. 12b, the MD tar cracking mechanism slightly increases the CO_2 yield in comparison with the simulation without secondary tar cracking, which corresponds well with the experimental result. However, the simple tar cracking model remarkably overpredicts the CO_2 production rate with the maximum difference reaching more than ten times the expected value. A similar trend is also seen in Fig. 12d for the C_2H_4 yield. Moreover, in Fig. 12c, the MD tar cracking model also captures the increase of the CH_4 production rate due to secondary tar cracking more reasonably than the simple tar cracking model. The above comparison illustrates that the developed MD tar cracking model significantly improves the accuracy of high-temperature pyrolysis simulation for thermally thick biomass particles under the tested condition.

To attain a clear understanding of the influence of tar cracking on the pyrolysis product yields, Fig. 13 presents the mass fraction contour for CO, and Fig. 14 shows that of levoglucosan ($C_6H_{10}O_5$), xylose monomer ($C_5H_8O_4$) and lumped-phenol ($C_{11}H_{12}O_4$) at 50 s, respectively, which are typical light gas and tar species generated from the primary pyrolysis of cellulose, hemicellulose and lignin based on the multistep kinetic scheme. In Fig. 13a, for the primary pyrolysis only case, a high CO concentration can be observed near the leeward side of the particle. When tar cracking is considered, the CO mass fraction inside the particle slightly increases, while outside the particle, much higher concentrations are observed, especially for the MD tar cracking model (Fig. 13c). From Fig. 14a1-a3, one can see that the levoglucosan mass fraction reaches 0.3 in the char layer for the primary pyrolysis case. When a simple tar cracking model is used, levoglucosan almost completely decomposes outside the particle, and the high concentration inside the particle also decreases. For the MD tar cracking model, the decomposition rate of levoglucosan is a little bit lower than that in the simple model. As a result, small amounts of levoglucosan can also be found in the gas phase outside the particle, but decrease rapidly in the high temperature flow field. For the xylose monomer distributions in Fig. 14b1-b3, the simple tar cracking model again predicts very fast decomposition both inside and outside the particle, while the MD tar cracking model gives rise to higher concentrations outside the particle (Fig. 14b3). This difference is likely caused by the variation of the intraparticle heating process due to the change of gas phase thermophysical properties (e.g., density and heat capacity) from tar cracking, which is in line with observations from our previous work [42]. Actually, the variation also results in flow-field unsteadiness outside the particle, which can be seen from the fluctuations in the species yield history (Fig. 12). The lumped-phenol distribution in Fig. 14c1-c3 also illustrates that the tar cracking outside the particle is very fast at 800 °C. Another interesting observation from Fig. 14 is that the tar species inside the particle do not show a uniform distribution. Some tar species such as levoglucosan and lumped phenol are mainly concentrated in the char layer, while other species like xylose monomer is mainly found in the central area of the particle.

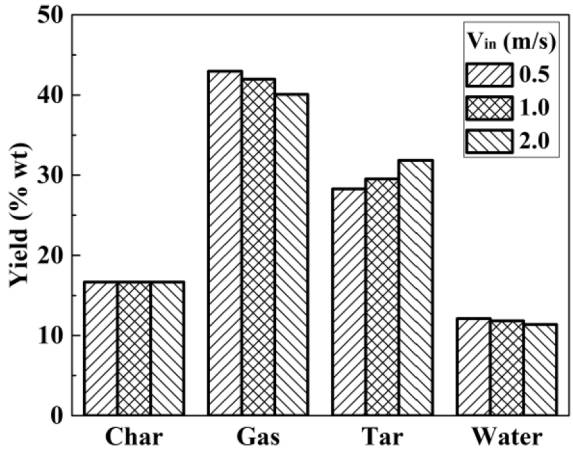

Fig. 16. Pyrolysis yields under different inflow velocities.

With the new algorithm, pyrolysis simulations under higher temperatures are further studied beyond the base case. Fig. 15a presents the char, gas, tar and water yields at 850, 950 and 1050 °C, respectively. Fig. 15b compares the CH_4, CO and CO_2 yields with increasing temperature. It is shown that the predicted species yields correspond well with experimental measurements both qualitatively and quantitatively, which are similar with that of the base case (800 °C). The above analysis demonstrates the feasibility of the MD tar cracking model, and the sensitive coupling between the tar decomposition and the advection/diffusion and heating processes inside the porous particle. In the high-temperature pyrolysis simulation of a thermally thick biomass particle, the coupling effect between devolatilization, tar cracking and heat transfer should not be ignored. This is one additional reason to conclude that, the simplified tar cracking model with a unified reaction rate is not suitable.

5. Discussion

In real applications of biomass combustion, the competition between tar cracking and oxidation plays an important role in the final product yields. From the comparisons in Fig. 14, it is clear that tar species with different cracking rates need different time to decompose, which influences the spatiotemporal development of their concentrations inside and outside the converting particle. Therefore, the residence time of tar in the flow field also influences the light gas generations. In this section, the effect of different inflow velocities on the pyrolysis product is discussed. Fig. 16 presents the pyrolysis yields at 800 °C under inflow velocities of 0.5, 1.0 and 2.0 m/s, respectively. It is shown that the light gas yield increases almost linearly with the increase of tar species residence time. Besides, for each light gas species, a similar increasing trend is also observed in the simulation (not shown). Fig. 17 further compares the species yield history of CO, CO_2, CH_4 and C_2H_4. Generally, the species evolution histories are very similar under different residence times. With

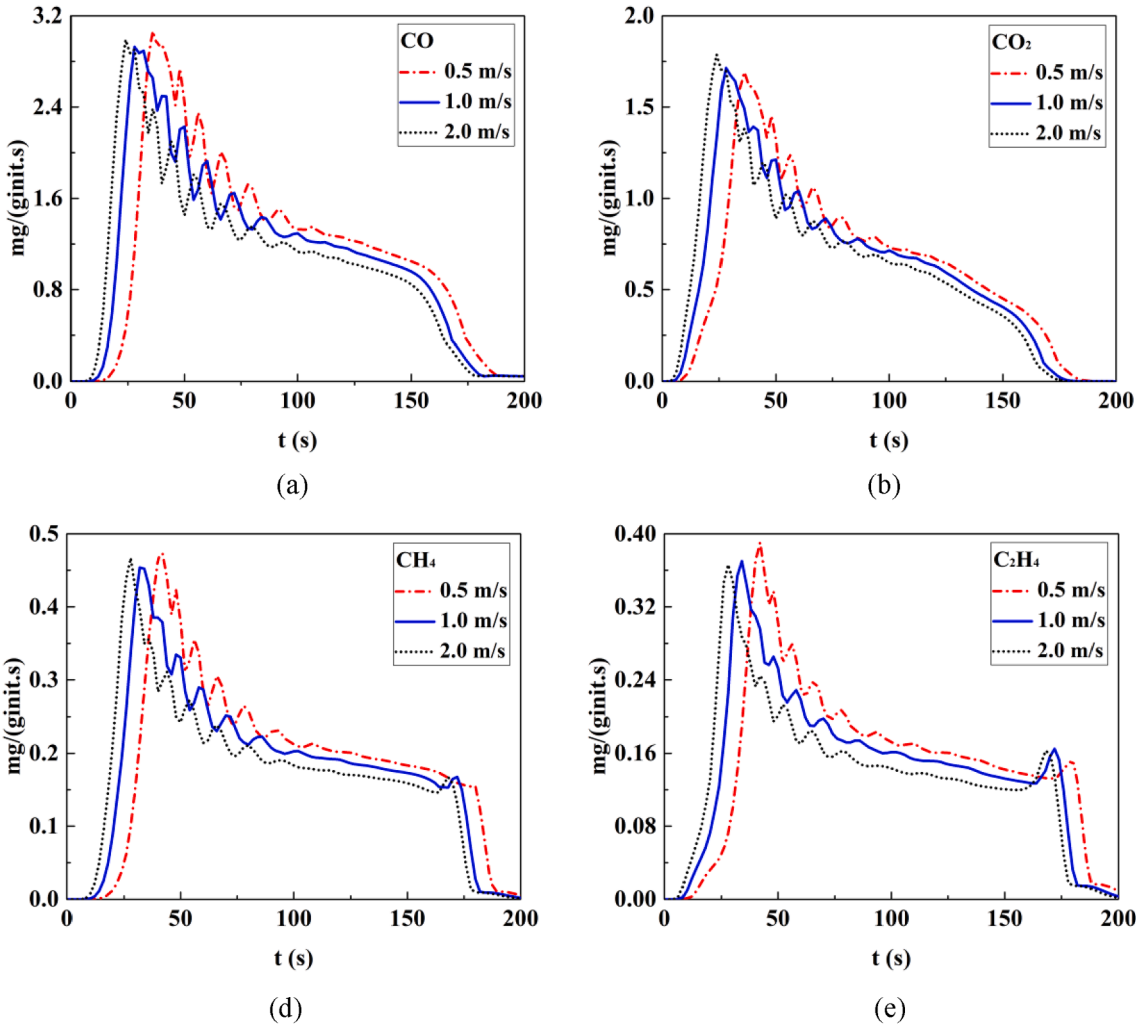

Fig. 17. Light gas production history under different inflow velocities.

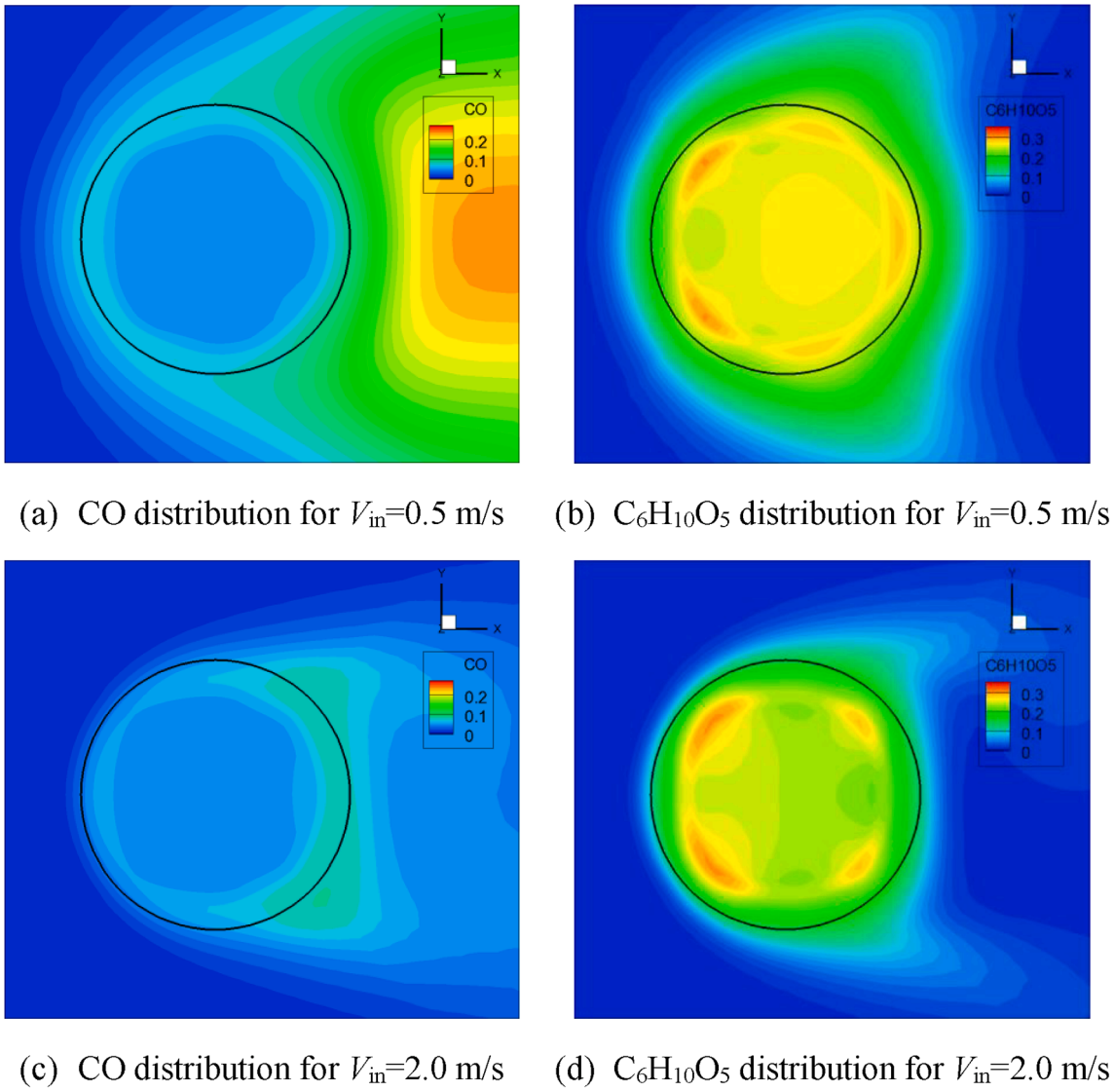

Fig. 18. Species mass fraction distributions at t = 50 s under different inflow velocities.

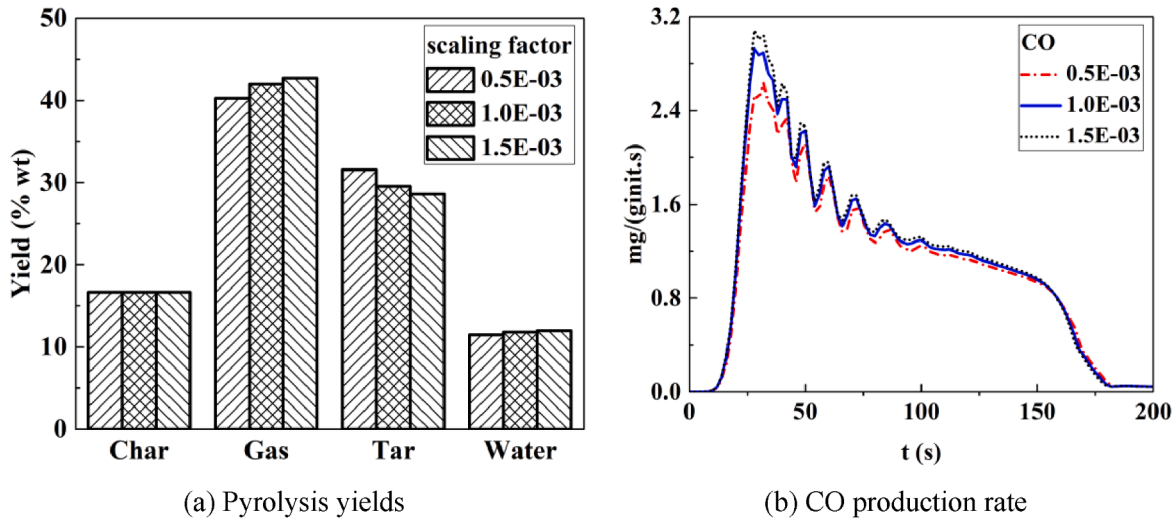

Fig. 19. Influence of pre-exponential scaling factor on the pyrolysis.

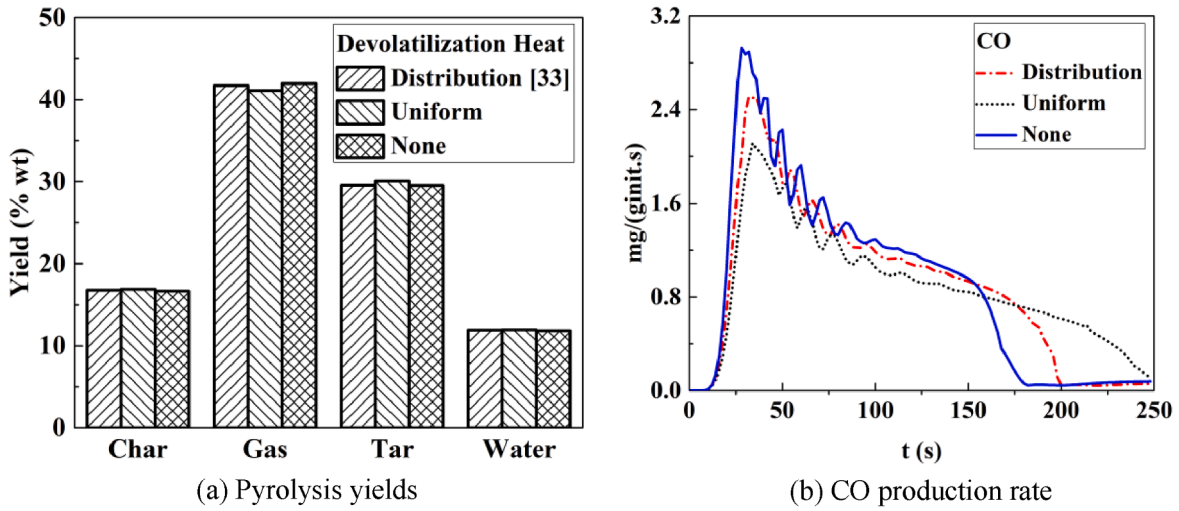

Fig. 20. Influence of devolatilization heat on the pyrolysis.

the increase of inflow velocity, the convective heating process is promoted, resulting in a faster devolatilization. However, the maximum formation rates of light gas species are almost the same under different inflow velocities. After the first releasing peak at around 25 s, the light gas yield is apparently promoted under a low inflow velocity (i.e. longer residence time). Fig. 18 compares the species distributions at 50 s for inflow velocity of 0.5 and 2.0 m/s. It is observed that, inside the particle, both light gas and tar yields do not show significant variations under different inflow velocities. However, the mass fraction outside the particle decreases much faster under a high inflow velocity.

Figs. 19-21 present the influence of several model parameters on the pyrolysis yields, including the pre-exponential scaling factor, the devolatilization heat and the initial specific surface area of the particle. For the impact of the pre-exponential scaling factor (Fig. 19), three cases (i.e., 0.5e-3, 1.0e-3 and 1.5e-3) are studied. It is seen that, when the scaling factor increases from 0.5e-3 to 1.0e-3, the tar yield decreases from 32% to 30% resulting in an approximately 2% increase in the light gas yield, while the char yield remains almost constant. The CO production rate in Fig. 19b shows a similar increasing trend to that of the total gas yield in Fig. 19a.

For the impact of the devolatilization heat (Fig. 20), three cases are compared: 1) distributed devolatilization heat, where the reaction heat, either endothermic or exothermic, is different for each of the biomass components (the values are taken from Gentile et al. [33]); 2) uniform devolatilization heat for all the pyrolysis reactions, where the reaction heat for each biomass component is set to a uniform value of 10 kcal/mol, which is of the same order of magnitude as that of Gentile et al. [33]; and 3) the current work without considering the devolatilization heat. The pyrolysis yields in Fig. 20a depict that the current prediction without considering the devolatilization heat is very close to the case of the distributed reaction heat, while the uniform case predicts a slightly higher tar yield and a lower light gas yield. The CO production rate in Fig. 20b illustrates that the endothermic characteristic of the pyrolysis reaction delays the heating process inside the biomass particle and thus results in a longer devolatilization period.

For the impact of the initial specific surface area (Fig. 21), three values of 3000, 6000 and 9000 m^2/m^3 are compared. Fig. 21a shows that the change in the specific surface area only causes a minor influence on the char and steam yields, while the tar yield decreases slightly from 30% at 3000 m^2/m^3 to 29% at 9000 m^2/m^3. The reason can be inferred from the CO production rate curves (Fig. 21b), where it is seen that, with increasing the initial specific surface area, the heating rate inside the particle is increased, changing the competitive pyrolysis reactions and thus resulting in a higher light gas yield. The above discussion provides important insight into the role of some of the key factors on the thermal decomposition of tar species in high-temperature pyrolysis, which lays a

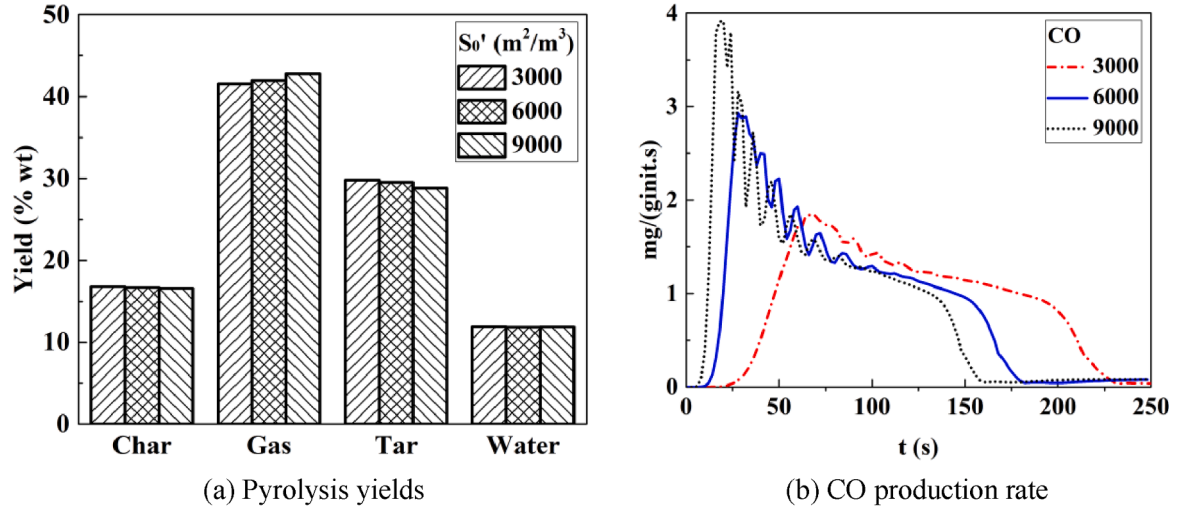

Fig. 21. Influence of initial specific surface area on the pyrolysis.

valuable foundation for further investigation of tar evolution in combustion and gasification.

6. Conclusions

A multistep kinetic scheme previously used and validated for low-temperature pyrolysis simulations is extended to high-temperature situations. The main contribution of the current work lies in the development of a new tar cracking model by using reactive molecular dynamic (MD) simulations. Each primary tar species from the multistep kinetic scheme is used to construct a microscale periodic pyrolysis system. The thermal decomposition of this microcell is then studied using NVT ensemble under different temperatures. From the information obtained during the initial stage of the decomposition, a one-step first-order Arrhenius-type tar cracking model is derived for each primary tar species. Thereafter, this MD tar cracking model is integrated with a thermally thick pyrolysis algorithm to form a particle-resolved high temperature pyrolysis model.

With the new algorithm, pyrolysis of a centimeter-sized beech wood particle at temperatures from 800 to 1050 °C is studied. In the base case (800 °C), the primary tar yield is reduced by nearly 50% due to secondary tar cracking (compared to simulations not accounting for secondary tar cracking). The predicted light gas yield reaches 42% of the initial mass, which is a little bit higher than the experimental measurement. Compared with the simple tar cracking model where a uniform reaction rate is assumed, the MD tar cracking model significantly improves the prediction accuracy of the pyrolysis yields. Especially, the relative difference in CO_2 yield reduces from more than 300% to 18%. Moreover, the error in the maximum light gas production rate is also greatly reduced. Simulations based on the MD tar cracking model reveal several details of secondary tar cracking in a thermally thick biomass particle that are difficult to observe in experiments. For example, it is shown that primary tar species such as levoglucosan and lumped-phenol mainly concentrate in the char layer and decompose very fast outside the particle, while other tar species like xylose monomer mainly concentrate in the center region of the particle and decompose slowly in the wake flow. In addition, simulations also illustrate that secondary tar cracking influences the diffusion/advection characteristics inside the particle and thus the heating process is also affected. The proposed model can be used to elucidate the formation and transformation of tar species from thermochemical conversion of biomass. This information is of great value in the process of better understanding and mitigating problems related to particulate emissions, surface degradation and overall process efficiencies.

Declaration of Competing Interest

The authors declare that they have no known competing financial interests or personal relationships that could have appeared to influence the work reported in this paper.

Acknowledgements

This work is financially supported by the Swedish Energy Agency (project number 46439-1), the Swedish Research Council Formas (project number Dnr 2017-00677), the Research Council of Norway (GASPRO - Fundamental insight into biomass gasification using experiments and mathematical modelling, 267916), the Swedish Centre for Biomass Gasification (SFC, project number P34721-3) and the Centre for Combustion Science and Technology (CECOST).

References

[1] Y. Ueki, T. Torigoe, H. Ono, R. Yoshiie, J.H. Kihedu, I. Naruse, Gasification characteristics of woody biomass in the packed bed reactor, Proc. Combust. Inst. 33 (2011) 1795–1800.
[2] J. Porteiro, D. Patiño, J. Moran, E. Granada, Study of a fixed-bed biomass combustor: influential parameters on ignition front propagation using parametric analysis, Energy Fuels 24 (2010) 3890–3897.
[3] F. Saleem, J. Harrisa, K. Zhanga, A. Harvey, Non-thermal plasma as a promising route for the removal of tar from the product gas of biomass gasification - A critical review, Chem. Eng. J. 382 (2020), 122761.
[4] S. Septien, S. Valin, C. Dupont, M. Peyrot, S. Salvador, Effect of article size and temperature on woody biomass fast pyrolysis at high temperature (1000–1400 °C), Fuel 97 (2012) 202–210.
[5] A.J. Josephson, R.R. Linn, D.O. Lignell, Modeling soot formation from solid complex fuels, Combust. Flame 196 (2018) 265–283.
[6] H. Thunman, M. Seemann, T.B. Vilches, J. Maric, D. Pallares, H. Ström, G. Berndes, P. Knutsson, A. Larsson, C. Breitholtz, O. Santos, Advanced biofuel production via gasification - lessons learned from 200 man-years of research activity with Chalmers' research gasifier and the GoBiGas demonstration plant, Energy Sci. Eng. 6 (2018) 6–34.
[7] S. Zhang, M. Asadullah, L. Dong, H. Tay, C. Li, An advanced biomass gasification technology with integrated catalytic hot gas cleaning. Part II: Tar reforming using char as a catalyst or as a catalyst support, Fuel 112 (2013) 646–653.
[8] A. Elorf, I. Bakhatar, M. Asbik, B. Sarh, P. Gillon, Fixed-bed biomass combustor: air mass flow rate and particles size effects on ignition front propagation of solid olive waste, Combust. Sci. Technol. 1–13 (2019).
[9] Z. Yao, X. He, Q. Hu, W. Cheng, H. Yang, C.H. Wang, A hybrid peripheral fragmentation and shrinking-core model for fixed bed biomass gasification, Chem. Eng. J. (2020).
[10] S. Kumar, S. Dasappa, Modeling and analysis of single particle conversion of biomass in a packed bed gasification system, Appl. Therm. Eng. 112 (2017) 1382–1395.
[11] Y.B. Yang, V.N. Sharifi, J. Swithenbank, L. Ma, L.I. Darvell, J.M. Jones, M. Pourkashanian, A. Williams, Combustion of a single particle of biomass, Energy Fuels 22 (1) (2008) 36–316.
[12] A.K. Biswas, K. Umeki, Simplification of devolatilization models for thermally thick particles: Differences between wood logs and pellets, Chem. Eng. J. 274 (2015) 181–191.
[13] R. Mehrabian, S. Zahirovic, R. Scharler, I. Obernberger, S. Kleditzsch, S. Wirtz, V. Scherer, H. Lu, L.L. Baxter, A CFD model for thermal conversion of thermally thick biomass particles, Fuel Process. Technol. 95 (2012) 96–108.
[14] M.P. Remacha, S. Jiménez, J. Ballester, Devolatilization of centimeter-sized biomass particles at high temperatures and heating rates, Part 2: Modeling and validation for thermally-thin and -thick regimes, Fuel 234 (2018) 707–722.
[15] K.S. Kung, A.F. Ghoniem, Multi-scale analysis of drying thermally thick biomass for bioenergy applications, Energy 187 (2019), 115989.
[16] C. Di Blasi, Modeling chemical and physical processes of wood and biomass pyrolysis, Prog. Energy Combust. Sci. 34 (2008) 47–90.
[17] M.A. Gómez, J. Porteiro, D. Patiño, J.L. Míguez, Fast-solving thermally thick model of biomass particles embedded in a CFD code for the simulation of fixed-bed burners, Energy Convers. Manage. 105 (2015) 30–44.
[18] T. Li, H. Thunman, H. Ström, A fast-solving particle model for thermochemical conversion of biomass, Combust. Flame 213 (2020) 117–131.
[19] H. Lu, W. Robert, G. Peirce, B. Ripa, L.L. Baxter, Comprehensive study of biomass particle combustion, Energy Fuels 22 (2008) 2826–2839.
[20] W.A.M.K.P. Wickramaarachchi, M. Narayana, Pyrolysis of single biomass particle using three-dimensional computational fluid dynamics modelling, Renewable Energy 146 (2020) 1153–1165.
[21] L. Lu, X. Gao, M. Shahnam, W.A. Rogers, Bridging particle and reactor scales in the simulation of biomass fast pyrolysis by coupling particle resolved simulation and coarse grained CFD-DEM, Chem. Eng. Sci. 216 (2020), 115471.
[22] G.M. Karthik, V.V. Buwa, Effect of particle shape on catalyst deactivation using particle-resolved CFD simulations, Chem. Eng. J. 377 (2019), 120164.
[23] S. Schulze, A. Richter, M. Vascellari, A. Gupta, B. Meyer, P.A. Nikrityuk, Novel intrinsic-based submodel for char particle gasification in entrained-flow gasifiers: Model development, validation and illustration, Appl. Energy 164 (2016) 805–814.
[24] N. Vorobieva, A. Beckera, H. Kruggel-Emdenb, A. Panahic, Y.A. Levendisc, M. Schiemann, Particle shape and Stefan flow effects on the burning rate of torrefied biomass, Fuel 210 (2017) 107–120.
[25] W.N.R.W. Isahak, M.W.M. Hisham, M.A. Yarmo, T.Y. Hin, A review on bio-oil production from biomass by using pyrolysis method, Renewable Sustainable Energy Rev. 16 (2012) 5910–5923.
[26] N. Rakesh, S. Dasappa, A critical assessment of tar generated during biomass gasification - Formation, evaluation, issues and mitigation strategies, Renewable Sustainable Energy Rev. 91 (2018) 1045–1064.
[27] M.G. Nugraha, H. Saptoadi, M. Hidayat, B. Andersson, R. Andersson, Particle modelling in biomass combustion using orthogonal collocation, Appl. Energy 255 (2019), 113868.
[28] R.S. Miller, J. Bellan, A generalized biomass pyrolysis model based on superimposed cellulose, hemicellulose and lignin kinetics, Combust. Sci. Technol. 126 (1–6) (1997) 97–137.
[29] A. Gómez-Barea, B. Leckner, Modeling of biomass gasification in fluidized bed, Prog. Energy Combust. Sci. 36 (4) (2010) 444–509.
[30] S. Hameed, A. Sharma, V. Pareek, H. Wu, Y. Yu, A review on biomass pyrolysis models: Kinetic, network and mechanistic models, Biomass Bioenergy 123 (2019) 104–122.
[31] P.E.A. Debiagi, C. Pecchi, G. Gentile, A. Frassoldati, A. Cuoci, T. Faravelli, E. Ranzi, Extractives extend the applicability of multistep kinetic scheme of biomass pyrolysis, Energy Fuels 29 (2015) 6544–6555.

[32] P.E.A. Debiagi, M. Trinchera, A. Frassoldati, T. Faravelli, R. Vinu, E. Ranzi, Algae characterization and multistep pyrolysis mechanism, J. Anal. Appl. Pyrolysis 128 (2017) 423–436.
[33] G. Gentile, P.E.A. Debiagi, A. Cuoci, A. Frassoldati, E. Ranzi, T. Faravelli, A computational framework for the pyrolysis of anisotropic biomass particles, Chem. Eng. J. 321 (2017) 458–473.
[34] P. Mellin, E. Kantarelis, W. Yang, Computational fluid dynamics modeling of biomass fast pyrolysis in a fluidized bed reactor, using a comprehensive chemistry scheme, Fuel 117 (2014) 704–715.
[35] S. Wang, G. Dai, H. Yang, Z. Luo, Lignocellulosic biomass pyrolysis mechanism: A state-of-the-art review, Prog. Energy Combust. Sci. 62 (2017) 33–86.
[36] B. Zhou, A. Dichiara, Y. Zhang, Q. Zhang, J. Zhou, Tar formation and evolution during biomass gasification: An experimental and theoretical study, Fuel 234 (2018) 944–953.
[37] S.H. Mushrif, V. Vasudevan, C.B. Krishnamurthy, B. Venkatesh, Multiscale molecular modeling can be an effective tool to aid the development of biomass conversion technology: A perspective, Chem. Eng. Sci. 121 (2015) 217–235.
[38] A.C.T. van Duin, S. Dasgupta, F. Lorant, W.A. Goddard III, ReaxFF: A reactive force field for hydrocarbons, J. Phys. Chem. A 105 (2001) 9396–9409.
[39] F. Castro-Marcano, A.M. Kamat, M.F. Russo Jr, A.C.T. van Duin, J.P. Mathews, Combustion of an Illinois No. 6 coal char simulated using an atomistic char representation and the ReaxFF reactive force field, Combust. Flame 159 (2012) 1272–1285.
[40] M. Zheng, Z. Wang, X. Li, X. Qiao, W. Song, L. Guo, Initial reaction mechanisms of cellulose pyrolysis revealed by ReaxFF molecular dynamics, Fuel 177 (2016) 130–141.
[41] C. Chen, L. Zhao, J. Wang, S. Lin, Reactive molecular dynamics simulations of biomass pyrolysis and combustion under various oxidative and humidity environments, Ind. Eng. Chem. Res. 56 (2017) 12276–12288.
[42] T. Chen, X. Ku, J. Lin, H. Ström, Pyrolysis simulation of thermally thick biomass particles based on a multistep kinetic scheme, Energy Fuels 34 (2) (2020) 1940–1957.
[43] T. Chen, X. Ku, J. Lin, CFD simulation of the steam gasification of centimeter sized char particle using thermally thick treatment, Combust. Flame 213 (2020) 63–86.
[44] T. Chen, X. Ku, J. Lin, H. Jin, Modeling of combustion for thermally thick biomass particles, Powder Technol. 353 (2019) 110–124.
[45] T. Chen, X. Ku, J. Lin, L. Fan, New pyrolysis model for biomass particles in a thermally thick regime, Energy Fuels 32 (9) (2018) 9399–9414.
[46] J. Blondeau, H. Jeanmart, Biomass pyrolysis at high temperatures: Prediction of gaseous species yields from an anisotropic particle, Biomass Bioenergy 41 (2012) 107–121.
[47] OpenCFD Ltd. OpenFOAM-The open source CFD toolbox-user guide (Version2.1.1). 2012.
[48] Materials Studio. [https://www.3ds.com/products-services/biovia/products/molecular-modeling-simulation/biovia-materials-studio].
[49] Sandia National Laboratories, LAMMPS. [https://lammps.sandia.gov].
[50] E. Salmon, A.C.T. van Duin, F. Lorant, P.M. Marquaire, W.A. GoddardIII, Thermal decomposition process in algaenan of Botryococcus braunii race L. Part 2: Molecular dynamics simulations using the ReaxFF reactive force field, Org. Geochem. 40 (3) (2009) 416–427.
[51] E. Salmon, A.C.T. van Duin, F. Lorant, P.M. Marquaire, W.A. GoddardIII, Early maturation processes in coal. Part 2: Reactive dynamics simulations using the ReaxFF reactive force field on Morwell Brown coal structures, Org. Geochem. 40 (12) (2009) 1195–1209.
[52] D. Hong, X. Guo, Molecular dynamics simulations of Zhundong coal pyrolysis using reactive force field, Fuel 210 (2017) 58–66.
[53] K. Chenoweth, A.C.T. van Duin, S. Dasgupta, W.A. Goddard III, Initiation mechanisms and kinetics of pyrolysis and combustion of JP-10 hydrocarbon jet fuel, J. Phys. Chem. A 113 (9) (2009) 1740–1746.
[54] M.R. Sørensen, A.F. Voter, Temperature-accelerated dynamics for simulation of infrequent events, J. Chem. Phys. 112 (2000) 9599.
[55] T. Lin, E. Goos, U. Riedel, A sectional approach for biomass: modelling the pyrolysis of cellulose, Fuel Process. Technol. 115 (2013) 246–253.
[56] X. Wang, J. Fang, B. Chen, J. Wang, J. Wu, D. Xia, Thermal decomposition characteristics and kinetics of methyl linoleate under nitrogen and oxygen atmospheres, Pet. Sci. 12 (2015) 518–524.
[57] A.M. Cortés, A.V. Bridgwater, Kinetic study of the pyrolysis of miscanthus and its acid hydrolysis residue by thermogravimetric analysis, Fuel Process. Technol. 138 (2015) 184–193.
[58] Y. Su, Y. Luo, Y. Chen, W. Wu, Y. Zhang, Experimental and numerical investigation of tar destruction under partial oxidation environment, Fuel Process. Technol. 92 (2011) 1513–1524.
[59] A. Cuoci, A. Frassoldati, T. Faravelli, E. Ranzi, Kinetic modeling of soot formation in turbulent nonpremixed flames, Environ. Eng. Sci. 25 (2008) 1407–1422.
[60] P.R. Johnson, R.K. Chakrabarty, B.M. Kumfer, Evaluation of semi-empirical soot models for nonpremixed flames with increased stoichiometric mixture fraction and strain, Combust. Flame 219 (2020) 70–85.
[61] G. Gauthier, T. Melkior, M. Grateau, S. Thiery, S. Salvador, Pyrolysis of centimetre-scale wood particles: new experimental developments and results, J. Anal. Appl. Pyrol. 104 (2013) 521–530.
[62] H. Ström, H. Thunman, CFD simulations of biofuel bed conversion: A submodel for the drying and devolatilization of thermally thick wood particles, Combust. Flame 169 (2013) 417–431.
[63] H. Tolvanen, T. Keipi, R. Raiko, A study on raw, torrefied, and steam-exploded wood: Fine grinding, drop-tube reactor combustion tests in N_2/O_2 and CO_2/O_2 atmospheres, particle geometry analysis, and numerical kinetics modeling, Fuel 176 (2016) 153–164.
[64] A. Richter, M. Kestel, P. Nikrityuk, Pore-resolved simulation of char particle combustion/gasification. Gasification processes: modeling and simulation, Wiley-VCH Verlag GmbH, Weinheim, 2014.